Facile Synthesis and Electrochemical Properties of Intermetallic PtPb Nanodendrites

Jingpeng Wang,[†,‡] Robert M. Asmussen,[†] Brian Adams,[†] Dan F. Thomas,[‡] and Aicheng Chen[†,*]

Department of Chemistry, Lakehead University, Thunder Bay, Ontario P7B 5E1, Canada, and Department of Chemistry, University of Guelph, Guelph, Ontario N1G 2W1, Canada

Received January 3, 2009. Revised Manuscript Received March 2, 2009

We report on a facile and environment-friendly route to synthesize intermetallic PtPb nanodendrites with controllable compositions. This involves a hydrothermal-assisted coreduction of Pt and Pb inorganic precursors by formic acid in aqueous solutions without the use of any surfactant or polymer. Our systematic structural characterization and in situ electrochemical infrared spectroscopic studies of the formed PtPb nanodendrites reveal that the underlying morphogenesis, resulting from the intermetallic phase evolution from a Pt-based face-centered cubic to a PtPb hexagonal type, is responsible for the significant improvement of electrocatalytic activities toward the electrochemical oxidation of formic acid. A foreign-particles-induced growth mechanism is proposed to account for the underlying dendritic growth process. The facile approach described in this study is further demonstrated to be universal for growing a variety of intermetallic nanodendrites, thus opening a door to develop and study novel nanodendritic materials.

Introduction

Dendrite and fractal structures are ubiquitous in nature, from leaf structures to whale bones. On the nanometer scale, dendrites and fractals are unique types of self-organized hyperbranched building blocks, which makes them promising candidates for the design and fabrication of new functional nanodevices and nanosystems. In the past decade, the design and synthesis of nanostructured materials along the "bottom-up" strategy have been essentially aimed at gaining accurate control over the size and shape of various inorganic nanoscale building blocks (such as nanocrystals, nanowires, nanobelts, nanotubes, and nanocages).[1−5] Future work has been suggested to explore more structural complexity in the nanocrystal family of building blocks,[6,7] such as self-organized hyperbranched subunits,[8−13] in that these unique nanostructures may be further hierarchically scaled up to build functional nanodevices and nanosystems. Dendritic and fractal structures, with major trunks and many hierarchical side branches, possess more complex and advanced structural characteristics than these simple building blocks and, hence, are identified as the most promising self-organized units among these advanced building blocks. To date, dendrites and fractals have been chemically fabricated for a variety of substances, such as metals,[14−17] metal oxides,[18,19] semiconductors,[20−23] and polymeric materials.[24] However, the design and synthesis of alloyed dendritic nanomaterials have been only sparsely addressed in the literature.[25−27] In addition, the majority of these reported works have focused on

* Corresponding author. Tel: 1-807-3438318. Fax: 1-807-3467775. E-mail: aicheng.chen@lakeheadu.ca.
† Lakehead University.
‡ University of Guelph.

(1) Burda, C.; Chen, X.; Narayanan, R.; El-Sayed, M. A. *Chem. Rev.* **2005**, *105*, 1025.
(2) Sun, S.; Murray, C. B.; Weller, D.; Folks, L.; Moser, A. *Science* **2000**, *287*, 1989.
(3) Patzke, G. R.; Krumeich, F.; Nesper, R. *Angew. Chem., Int. Ed.* **2002**, *41*, 2446.
(4) Murphy, C. J. *Science* **2002**, *298*, 2139.
(5) Glotzer, S. C.; Solomon, M. J. *Nat. Mater.* **2007**, *6*, 557.
(6) Wang, D.; Lieber, C. M. *Nat. Mater.* **2003**, *2*, 355.
(7) Colfen, H.; Mann, S. *Angew. Chem., Int. Ed.* **2003**, *42*, 2350.
(8) Chen, J.; Herricks, T.; Xia, Y. *Angew. Chem., Int. Ed.* **2005**, *44*, 2589.
(9) Hoefelmeyer, J. D.; Niesz, K.; Somorjai, G. A.; Tilley, T. D. *Nano Lett.* **2005**, *5*, 435.
(10) Jun, Y.; Lee, S.-M.; Kang, N.-J.; Cheon, J. *J. Am. Chem. Soc.* **2001**, *123*, 5150.
(11) Manna, L.; Milliron, D. J.; Meisel, A.; Scher, E. C.; Alivisatos, A. P. *Nat. Mater.* **2003**, *2*, 382.
(12) Milliron, D. J.; Hughes, S. M.; Cui, Y.; Manna, L.; Li, J.; Wang, L.-W.; Alivisatos, A. P. *Nature (London)* **2004**, *430*, 190.
(13) Chen, S.; Wang, Z. L.; Ballato, J.; Foulger, S. H.; Carroll, D. L. *J. Am. Chem. Soc.* **2003**, *125*, 16186.
(14) Song, Y.; Yang, Y.; Medforth, C. J.; Pereira, E.; Singh, A. K.; Xu, H.; Jiang, Y.; Brinker, C. J.; van Swol, F.; Shelnutt, J. A. *J. Am. Chem. Soc.* **2004**, *126*, 635.
(15) Xiao, J.; Xie, Y.; Tang, R.; Chen, M.; Tian, X. *Adv. Mater.* **2001**, *13*, 1887.
(16) Nakanishi, S.; Fukami, K.; Tada, T.; Nakato, Y. *J. Am. Chem. Soc.* **2004**, *126*, 9556.
(17) Ye, J.; Chen, Q.-W.; Qi, H.-P.; Tao, N. *Cryst. Growth Des.* **2008**, *8*, 2464.
(18) Cao, M.; Liu, T.; Gao, S.; Sun, G.; Wu, X.; Hu, C.; Wang, Z. L. *Angew. Chem.* **2005**, *117*, 4269.
(19) Balakrishnan, S.; Gun'ko, Y. K.; Perova, T. S.; Moore, R. A.; Venkatesan, M.; Douvalis, A. P.; Bourke, P. *Small* **2006**, *2*, 864.
(20) Yan, H.; He, R.; Johnson, J.; Law, M.; Saykally, R. J.; Yang, P. *J. Am. Chem. Soc.* **2003**, *125*, 4728.
(21) Dick, K. A.; Deppert, K.; Larsson, M. W.; Martensson, T.; Seifert, W.; Wallenberg, L. R.; Samuelson, L. *Nat. Mater.* **2004**, *3*, 380.
(22) Sukhanova, A.; Baranov, A. V.; Perova, T. S.; Cohen, J. H. M.; Nabiev, I. *Angew. Chem., Int. Ed.* **2006**, *45*, 2048.
(23) Li, G.-R.; Yao, C.-Z.; Lu, X.-H.; Zheng, F.-L.; Feng, Z.-P.; Yu, X.-L.; Su, C.-Y.; Tong, Y.-X. *Chem. Mater.* **2008**, *20*, 3306.
(24) Cho, S. O.; Lee, E. J.; Lee, H. M.; Kim, J. K.; Kim, Y. J. *Adv. Mater.* **2006**, *18*, 60.
(25) Qin, Y.; Song, Y.; Sun, N.; Zhao, N.; Li, M.; Qi, L. *Chem. Mater.* **2008**, *20*, 3965.
(26) Wen, X. G.; Xie, Y. T.; Mak, W. C.; Cheung, K. Y.; Li, X. Y.; Renneberg, R.; Yang, S. *Langmuir* **2006**, *22*, 4836.
(27) Wang, J.; Thomas, D. F.; Chen, A. *Chem. Commun.* **2008**, 5010.

10.1021/cm9000174 CCC: $40.75
Published on Web 04/02/2009

disordered alloys (i.e., random solid solutions). Ordered intermetallics that possess dendritic or fractal structures on a nanometer scale have hardly been investigated so far, not to mention any understanding or insight toward such structure's formation and associated properties.

The long-standing importance of intermetallic compounds and alloys lies in the fact that they possess a diverse range of chemical and physical properties, including ferromagnetism, superconductivity, shape-memory effects, catalytic activity, hydrogen storage, structural hardness, and corrosion resistance.[28] As a unique category, precious metals such as platinum and their alloys represent some of the most efficient catalysts used in fuel-cell technology, hydrogenation reaction, and the development of sensors and nanodevices.[29−33] In particular, pioneering work in the synthesis of Pt-based ordered intermetallic nanoparticles in fuel cell applications[34] has suggested that ordered intermetallic systems generally provide predictable control over structural, geometric, and electronic effects not afforded by disordered alloys (i.e., radom solid solutions such as Pt−Ru and Pt−Sn).

In general, the wet-chemical synthesis of monometallic nanocrystals involves metal precursors, reducing agents, and certain stabilizing or capping agents (such as surfactants or polymers). As for the fabrication of nanostructured intermetallics, it is even more challenging to choose an appropriate reducing agent such that it has the desired reducing potency to coreduce the mixed metal precursors simultaneously to produce a homogeneous product. Recently, we have systemically studied five different Pt-based nanoporous catalysts (e.g., Pt, Pt−Ru, Pt−Ir, Pt−Pd, and Pt−Pb), showing that the nanoporous Pt−Pb electrode greatly outperforms the other materials toward the electrochemical oxidation of formic acid.[35] In the present work, for the first time, we demonstrate a facile and reproducible route to synthesize intermetallic PtPb dendritic nanostructures with controllable compositions. This involves a hydrothermal-assisted coreduction of Pt and Pb inorganic precursors by formic acid in aqueous solutions without the use of any surfactant or polymer. A foreign-particle-induced growth mechanism is proposed to account for the underlying dendritic growth process, which is further demonstrated to be universal for growing a variety of intermetallic dendritic building blocks.

Experimental Section

Synthesis of Pt-Containing Nanostructures. A Ti plate (99.2%, 1.25 cm × 0.80 cm × 0.5 mm) was washed in acetone followed by Nanopure water (18.2 MΩ cm) and then etched in an 18 wt % HCl solution at 85 °C for 10 min. The etched Ti substrate was transferred into a Teflon-lined autoclave containing 10 mL of an aqueous mixture of inorganic metal precursors and formic acid (Aldrich, 96.0%). The metal precursors used in this study were $H_2PtCl_6 \cdot 6H_2O$, $Pb(NO_3)_2$, $Bi(NO_3)_3 \cdot 5H_2O$, $HAuCl_4 \cdot xH_2O$, $RuCl_3 \cdot 3H_2O$, and $PdCl_2$, all of which were used as received from Aldrich and added in the desired stoichiometric amounts from their stock solutions. In particular, the solvent for the stock solutions of $Bi(NO_3)_3$ and $PdCl_2$ was diluted aqueous HNO_3 and HCl solutions, respectively, in order to improve solubility. Otherwise, Nanopure water was always used as a solvent. In the case of fabricating PtAu and PdRu dendrites, the starting solution pH was adjusted by ammonium hydroxide solution to 5.5−6.5 before hydrothermal treatment. For ease of comparison, the initial concentration of the H_2PtCl_6 precursor was kept constant (5.4 mM) in all cases. The autoclave was heated to 180 °C and held there for 8 h. After cooling to room temperature, the deposit-coated Ti plate was rinsed with pure water.

Physical Characterization of the Synthesized Nanostructures. The surface morphology of the synthesized samples was characterized using scanning electron microscopy (SEM) (JEOL JSM 5900LV) and transmission electron microscopy (TEM) (JEOL 2010F). Surface composition was investigated by an energy dispersive X-ray spectrometer (EDS) (Oxford Links ISIS) and X-ray photoelectron spectroscopy (XPS) (Omicron EA-125 energy analyzer and a multichannel detector) using a monochromatic Mg Kα X-ray source ($h\nu = 1253.6$ eV). Surface compositions based on quantitative EDS analysis are reported as average values of readings taken at five different spots on each sample surface. All binding energies reported were corrected using the C 1s peak at 284.5 eV as an internal standard. Atomic sensitivity factors were employed for calculating the surface metallic compositions from the integrated peak areas. The X-ray diffraction (XRD) patterns of the as-prepared samples were recorded using a Philips PW 1050-3710 diffractometer with Cu Kα radiation.

Electrochemical and Spectroscopic Characterization of the Synthesized Nanostructures. Cyclic voltammetry (CV) was carried out using a three-electrode cell system. In all cases, a platinum coil was used as the counter electrode and was flame annealed before each experiment. The working electrode was the as-synthesized Ti-supported PtPb catalysts. A saturated calomel electrode (SCE) was used as the reference and connected to the investigated electrolyte through a salt bridge. All potentials reported in this paper refer to the SCE reference electrode. Data acquisition and analysis were performed with a Solartron 1287 potentiostat using the software CorrWare. The geometric surface area of each electrode was used to calculate the current density. All solutions were deaerated with ultrapure argon (99.999%) before measurements, and argon was passed over the top of the solution during the experiments. All measurements were conducted at room temperature (20 ± 2 °C).

All in situ attenuated total reflection-Fourier transform infrared spectroscopy (ATR-FTIR) experiments were performed using a Nicolet Fourier transform infrared spectrometer with a liquid N_2 cooled MCT detector. The spectroelectrochemical cell consisted of a Teflon chamber with a ZnSe hemisphere window sealed on the bottom. The synthesized nanodendrites were suspended in pure water with the aid of ultrasonic treatment and then coated onto the ZnSe window. The incidence angle of the IR beam was controlled with a variable angle homemade accessory and was set to 60° for all experiments. The spectra were recorded using a single potential step procedure in which the electrode potential was controlled by a potentiostat and increased in steps of +0.10 V. All interferograms were acquired at 4 cm^{-1} resolution, and 400 scans were added and

(28) Ferrando, R.; Jellinek, J.; Johnston, R. L. *Chem. Rev.* **2008**, *108*, 845.
(29) Wang, J.; Thomas, D. F.; Chen, A. *Anal. Chem.* **2008**, *80*, 997.
(30) Koczkur, K.; Yi, Q.; Chen, A. *Adv. Mater.* **2007**, *19*, 2648.
(31) Bock, C.; Paquet, C.; Couillard, M.; Botton, G. A.; MacDougall, B. R. *J. Am. Chem. Soc.* **2004**, *126*, 8028.
(32) Babu, P. K.; Kim, H. S.; Oldfield, E.; Wieckowski, A. *J. Phys. Chem. B* **2003**, *107*, 7595.
(33) Teng, X.; Maksimuk, S.; Frommer, S.; Yang, H. *Chem. Mater.* **2007**, *19*, 36.
(34) Casado-Rivera, E.; Volpe, D. J.; Alden, L.; Lind, C.; Downie, C.; Vaquez-Alvarez, T.; Angelo, A. C. D.; DiSalvo, F. J.; Abruña, H. D. *J. Am. Chem. Soc.* **2004**, *126*, 4043.
(35) Wang, J.; Holt-Hindle, P.; MacDonald, D.; Thomas, D. F.; Chen, A. *Electrochim. Acta* **2008**, *53*, 6944.

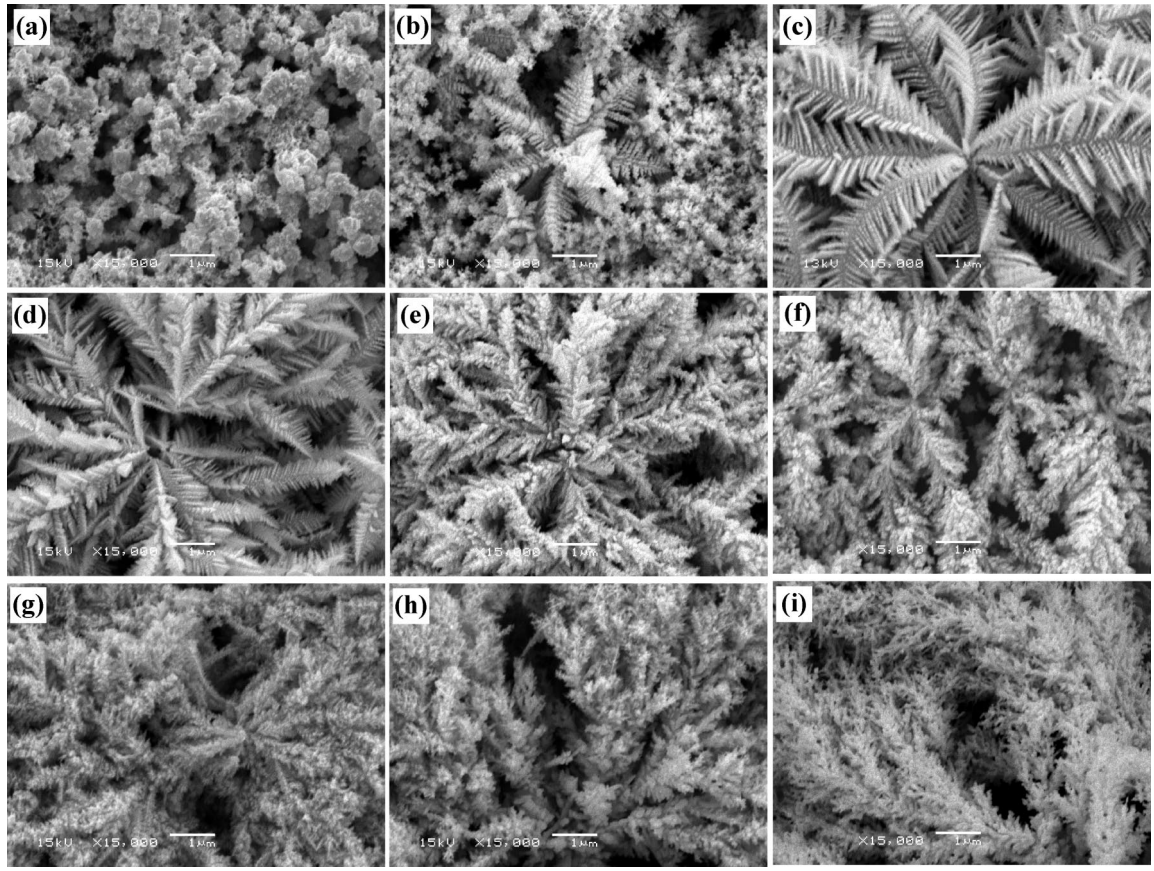

Figure 1. Morphology of the as-synthesized Pt-containing nanostructures. SEM images shown with the normalized Pt:Pb atomic ratio determined by quantitative EDS analysis: (a) 100:0, (b) 99.5:0.5, (c) 97.5:2.5, (d) 95:5, (e) 91:9, (f) 80:20, (g) 70:30, (h) 60:40, and (i) 50:50. All scale bars are 1 μm.

averaged. The interferograms were shown in terms of relative change of the electrode reflectivity, which is defined as $\Delta R/R = (R(E_2) - R(E_1))/R(E_1)$, where $R(E_1)$ and $R(E_2)$ are the thin films' reflectivity at potentials E_1 and E_2, respectively. The spectra recorded at $E_1 = -0.20$ V was used as reference.

Results and Discussion

For the ease of comparison, the intermetallic composition of PtPb materials is always expressed in the normalized atomic ratio of Pt:Pb throughout our discussion. Figure 1 shows the typical SEM images of the synthesized PtPb materials with Pb atom % gradually increased from 0% to 50%. As a common feature for all the compared samples, these deposits were always found to be uniformly distributed across the entire substrate, and the average Pt:Pb ratio of each sample determined by EDS analysis accurately matches that of the initial precursors. Micrograph a presents the typical morphology of pure Pt particles prepared by the as-described hydrothermal process. It can be seen that there is only agglomerated particles of irregular round shapes deposited on the substrate, without any sign of dendritic structure. However, with only trace amounts of Pb^{2+} cations, about 0.5 atom % compared to Pt cations, added to the starting solution, the resultant deposits, shown in Figure 1b, surprisingly contain dendritic segments surrounded by spongelike particles. The formed dendrite has main trunks of about 2 μm in length and secondary side branches 100−500 nm long. Characterized by EDS analysis, the dendritic structures ubiquitously contain ca. 0.5−1.0 atom % Pb and 99.5−99.0 atom % Pt, and the remaining spongelike particles are made of 100% Pt. On the basis of the minority surface population and the composition of such dendrites, it is evident that the trace amount of lead cations, although not capable of producing massive quantities of dendrites, are responsible for triggering the dendritic growth of Pt species.

Subsequent increase of the Pb concentration in the mixture of precursors resulted in large-scale production of dendritic and fractal-like morphologies. When the inorganic precursors were mixed as Pt:Pb (97.5:2.5), the produced deposits, illustrated in Figure 1c, have ordered dendritic characteristics with primary main trunks of 4−5 μm, secondary side branches of 0.2−1.6 μm, and tertiary side branches under 200 nm in length. Another interesting feature of the main trunks is that they have a certain degree of symmetry: approximately 10 main trunks grow out three-dimensionally from the same seed at the bottom end. When the Pb^{2+} concentration doubles to 5 atom %, the formed dendrites shown in Figure 1d break their macroscopic growth symmetry to some extent, in that fewer main trunks share the same growing seed at the bottom end and the length of both the trunks and side branches has shrunk about 20% compared to the dendrites seen in Figure 1c [PtPb (97.5:2.5)]. When the lead content was further increased to 9%, 20%, 30%, and 40%, respectively, the produced dendrites became more and more disordered and grainy on their side branches, demonstrating a clear evolution from tip-splitting branchings (Figure 1e and f) to dense-branching morphology (Figure

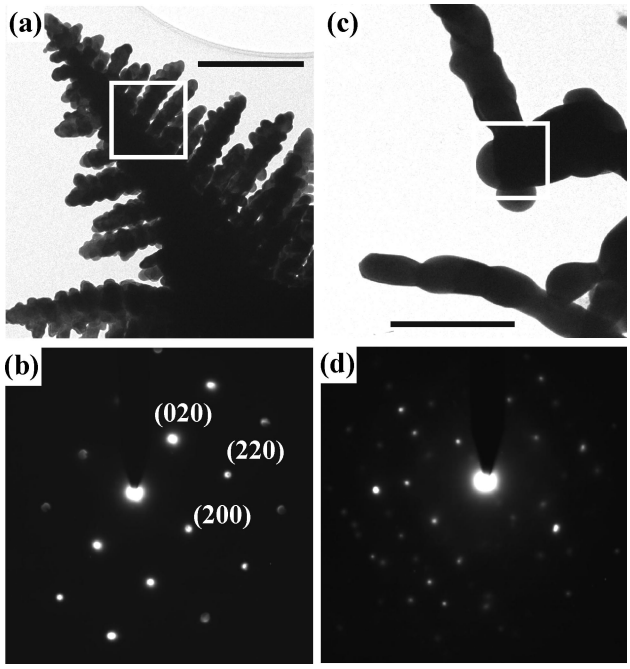

Figure 2. TEM images of PtPb (95:5) (a) and PtPb (50:50) (c) nanostructures, and SAED patterns (b and d) recorded from the white square areas shown in parts a and c, respectively. Both scale bars in parts a and c are 200 nm.

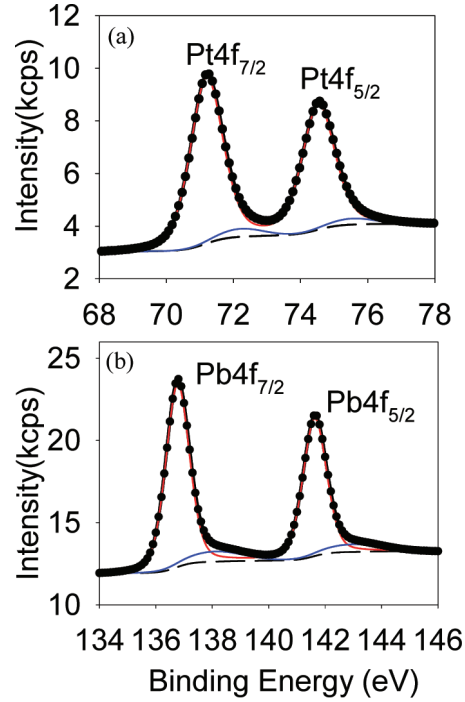

Figure 3. XPS spectra of the Pt 4f (a) and Pb 4f (b) regions for the as-synthesized PtPb (50:50) sample. The dots, dashed lines, and red, blue, and black solid lines represent the raw data, baseline, individual components (zero and high oxidation states) and total fit, respectively.

1g) and finally to fractal-like structure (Figure 1h). When the Pt and Pb precursors were mixed at an equimolar ratio, the produced deposits, shown in Figure 1i, appear as bunches of branched filaments that are still grown in fractal-like patterns. On this microscopic scale, the morphogenesis of the produced deposits, from the well-defined hierarchical dendrites, via intermediate dendritic and fractal-like structures, finally to branched fractal-like filaments, strongly indicates some dramatic changes in the nucleation and growth rate caused by the systematic variations in Pt:Pb compositions during the crystallization process.

Figure 2 presents the typical TEM images and SAED patterns of two selected PtPb specimens, PtPb (95:5) and PtPb (50:50). A typical secondary side branch of PtPb (95:5) dendrite is shown in Figure 2a. It can be clearly seen that the whole side branch resembles the morphology of a certain species of pine trees with conical shape from top to bottom. The hierarchical tertiary branches build up in parallel to each other and nearly perpendicularly (90°) to the subtrunk (i.e., the secondary branch); the quadratic branches, seen as long grains grown on tertiary branches, are also situated perpendicularly (90°) to their individual tertiary branch. The smallest discernible grains are about 10 nm in diameter. The corresponding SAED pattern of this dendritic segment, shown in Figure 2b, possesses a unique square symmetry viewed along [001] zone axis. The indexed diffraction spots consistently reveal the face-centered cubic (fcc) phase and the single crystalline nature of the synthesized PtPb (95:5) dendrite. This further indicates that the preferential growth direction of the subtrunks and hierarchical branches is along the ⟨100⟩ direction. Figure 2c shows the PtPb (50:50) nanostructures after severe ultrasonication treatment. The building units of the branched filaments are nodulated nanorods with each node serving as a joining point, which allows the rod to grow in different directions. The corresponding SAED pattern (Figure 2d) confirms a single crystalline feature of the formed nanorod; the complicated diffraction pattern is due to structure overlapping at the node joint. In addition, there is no distinguishable phase segregation found as individual Pt or Pb entities among the grains, revealing that these two elements form ordered intermetallic structures on the nanometer scale.

Our X-ray photoelectron spectroscopic (XPS) studies (Figure 3) reveal a high percentage of metallic species and small fractions of Pt and Pb in high oxidation states, demonstrating a highly effective reduction of metal precursors by the hydrothermal process. The two 4f binding states of zero valence Pt^0 are identified as $4f_{7/2}$ and $4f_{5/2}$ at 71.2 and 74.5 eV, respectively, and the position of the Pb^0 $4f_{7/2}$ spectral line is found at 136.8 eV. This indicates a small shift compared to pure polycrystalline Pt and Pb. This is in good agreement with previous study: no significant electronic interaction between Pt and Pb upon the formation of an intermetallic alloy.[36] The surface atomic Pt:Pb ratio was calculated to be 50.3:49.7, consistent with the EDS analysis and the initial stoichiometry of the mixed precursors.

Figure 4a shows a series of X-ray diffraction (XRD) patterns. In the spectra of the PtPb (x:100 − x) nanostructures with x varied from 100 to 75, all peaks, except those contributed from the Ti substrate, can be indexed to fcc crystal structures. Interestingly, when the Pt content drops to 70 atom %, a set of new diffraction patterns appears; their intensity gradually increases along with the further decrease

(36) Blasini, D. R.; Rochefort, D.; Fachini, E.; Alden, L. R.; DiSalvo, F. J.; Cabrera, C. R.; Abruna, H. D. *Surf. Sci.* **2006**, *600*, 2670.

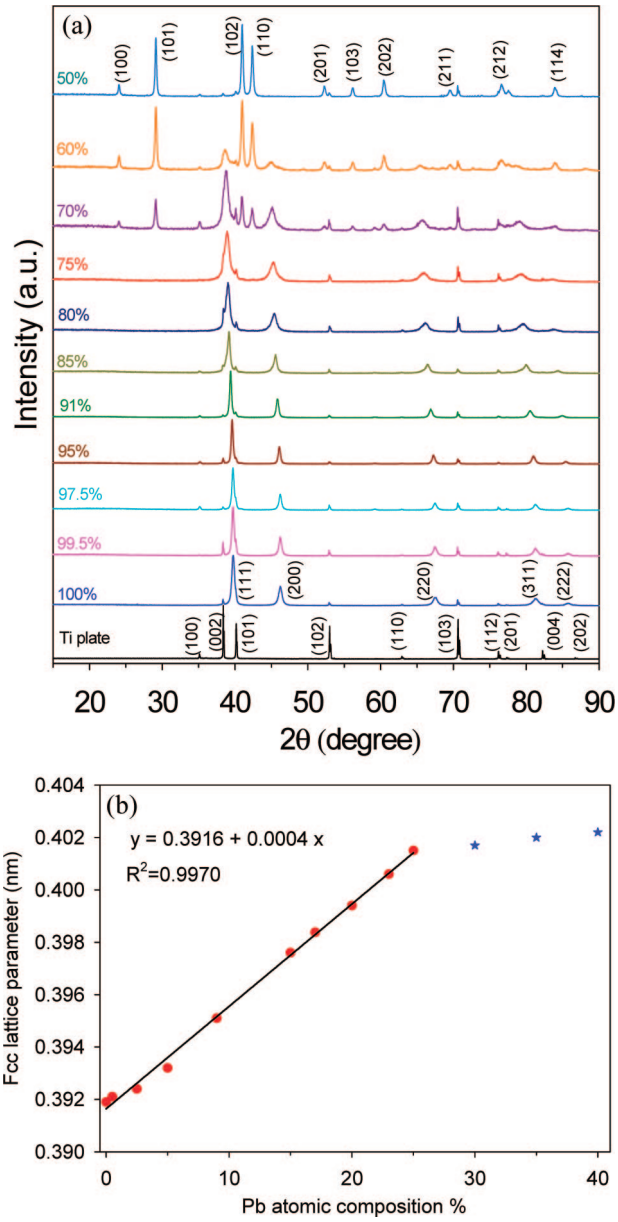

Figure 4. (a) XRD spectra of the as-synthesized Pt-containing nanomaterials and Ti substrate (normalized atomic composition of Pt was labeled on each spectrum). (b) Vegard's plot: dependence of the fcc lattice parameters calculated from the (220) peaks of each spectrum in part a on the normalized atomic composition of Pb; the linear regression fit to Vegard's law is shown as a solid line through regions of 0−25 atom % of Pb.

of the Pt percentage. The Pt-based fcc patterns completely vanish and these new diffraction patterns prevail in the spectrum of PtPb (50:50). These new XRD patterns belong to the PtPb hexagonal NiAs crystal structure (JCPDS file no. 06-0374, space group: $P6_3/mmc$, $a = 0.424$ nm, $c = 0.548$ nm). As seen from the spectrum of Pt (100 atom %) up to that of PtPb (75:25), the 2θ values of all the fcc crystal planes have a slight and consistent shift to lower values. For instance, the fcc (220) of Pt (100 atom %) has the peak 2θ value at 67.51°, whereas the fcc (220) of PtPb (75:25) has it at 65.70°. This characteristic of subtle peak shift to lower 2θ values essentially corresponds to the increased d-spacing values and dilated lattice constants due to the gradual incorporations of Pb atoms into the Pt-based fcc crystal lattice. It is worth noting that, in all the spectra with the

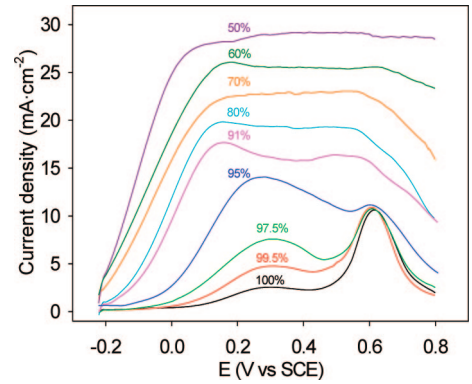

Figure 5. Forward-scanning cyclic voltammograms of Pt-containing nanomaterials in a solution of 0.1 M formic acid + 0.1 M H_2SO_4 at a potential scan rate of 20 mV/s (normalized atomic composition of Pt for each electrode is labeled on the corresponding curve).

presence of the hexagonal PtPb phase, the ratio between the intensities of the (102) and (101) diffraction peaks was higher than the standard value (1.2 versus 0.8), indicating that the hexagonal PtPb (50:50) dendritic filaments were abundant in {102} facets; thus their {102} planes tended to be preferentially oriented parallel to the surface of the supporting substrate.

The calculated fcc lattice parameter presented in Figure 4b follows the Vegard's type law, which is frequently observed with binary metallic alloys. This important finding reveals how the crystal lattice alters itself with the systematic change of bimetallic compositions. When Pb was increased to over 25 atom %, a new crystalline phase hexagonal PtPb appeared and coexisted with some intermediate fcc crystal phases, showing that the PtPb (75:25)−Pt_3Pb intermetallic structure exists as a critical phase, beyond which the fcc crystal lattice no longer accommodates more incoming Pb atoms without adopting a new energetically favorable lattice structure, the hexagonal PtPb phase. In those cases where such systematically varied intermetallic lattice facets are exposed to incoming molecular adsorbates, a certain degree of changes in the chemisorption behavior of the adsorbates is expected due to the surface-specific crystalline symmetries.

We further studied the dependence of the PtPb properties on their crystal structures and compositions using a characteristic electrocatalysis process, the electrochemical oxidation of formic acid. Figure 5 shows the forward-scanning cyclic voltammograms of the synthesized PtPb nanostructures. The gradually increased Pb content significantly enhanced the current densities in the low potential regions (from −0.10 to +0.50 V). On the basis of the well-accepted dual reaction pathways,[37] we conclude that the oxidation of formic acid on the PtPb (x:100 − x) nanostructures with x varied from 100 to 95 mainly follows the dehydration path, which involves the generation of surface-poisoning CO species as an intermediate product, thus resulting in small current under low electrode potentials. Nevertheless, the increase of current for 0.5, 2.5, and 5 atom % of Pb can be ascribed to the effect of crystal lattice dilation caused by the gradual addition of

(37) Markovic, N. M.; Gasteiger, H. A.; Ross, P. N.; Jiang, X.; Villegas, I.; Weaver, M. J. *Electrochim. Acta* **1995**, *40*, 91.

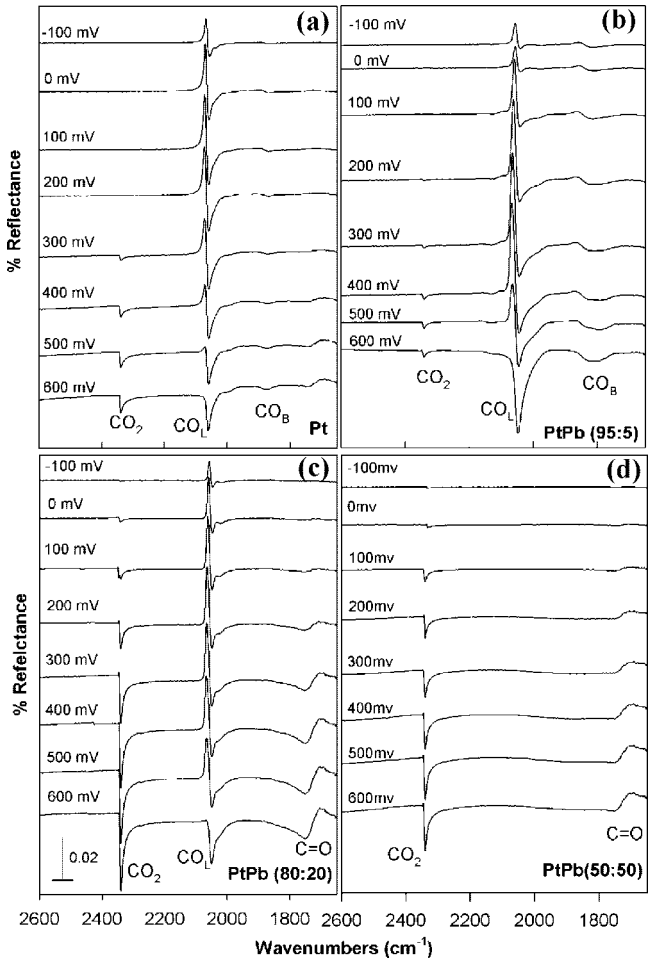

Figure 6. In situ electrochemical ATR-FTIR spectra for formic acid oxidation (0.1 M formic acid + 0.1 M H_2SO_4) on Pt particles (a) and nanodendrites of PtPb (95:5) (b), PtPb (80:20) (c), and PtPb (50:50) (d); the spectrum recorded at −0.2 V was used as reference.

Pb atoms into the Pt crystal structure, thus resulting in less and less CO molecules chemisorbed through the bridge or 3-fold hollow bonding sites of the Pt surface.[38] Such ensemble/ligand effect is obviously further enhanced with higher percentages of Pb (9−50 atom %). These electrodes not only possess enhanced current densities but also have much lower onset potential for formic acid oxidation compared to the Pt particles.

In order to clarify and confirm the aforementioned reaction mechanism, we further employed an in situ electrochemical ATR-FTIR technique, which is capable of detecting surface-adsorbed intermediate species with high sensitivity.[39,40] Considering the differences in both the electrocatalytic activity and crystal structures, four different PtPb (x:100 − x) deposits were chosen: (i) Pt particles, (ii) PtPb (95:5), (iii) PtPb (80:20), and (iv) PtPb (50:50). Figure 6a shows a series of potential-dependent FTIR spectra for formic acid oxidation on monometallic Pt particles. From −100 to +500 mV, each related spectrum has a large inverted bipolar peak at around 2065 cm^{-1}, which is attributed to the potential-dependent IR absorption of the linearly bonded CO species (CO_L) on the catalysts' surfaces. It is worth noting that the negative lobes of the bipolar peaks are potential-independent and that the positive lobes of the bipolar peaks shift to higher frequency with the increasing electrode potential and vanish completely at +600 mV. Such inverted bipolar phenomena originates from the electrochemical Stark tuning effect and usually can be seen on nanostructured thin films of platinum metals and alloys.[41,42] Meanwhile, a relatively small but broad negative-going band centered near 1815 cm^{-1} can be assigned to the IR absorption of bridge-bonded CO species (CO_B). The CO_2 species, produced from the oxidation of CO_{ads}, are characterized by the negative-going band at 2340 cm^{-1} starting from +300 mV. The process of converting CO to CO_2 is consistent with the increase in current density from +300 to +600 mV in the CV spectrum of 100 atom % Pt shown in Figure 5.

In the case of PtPb (95:5) nanodendrites (Figure 6b), the peaks representing CO_B and CO_L species are essentially similar to those observed for 100 atom % Pt (Figure 6a). In contrast, the formation of CO_2 on PtPb (95:5) nanodendrites, indicated by the small negative-going band at 2340 cm^{-1}, starts from +0.20 V, being 100 mV more negative than that of 100 atom % Pt. Such evidence infers the origin of the enhanced current density previously shown in Figure 5, in part suggesting that the improved catalytic activity of PtPb (95:5) nanodendrites compared to Pt particles is due to the incorporated 5 atom % of Pb. However, it appears that the oxidation of formic acid on PtPb (95:5) nanodendrites still proceeds via the dehydration pathway, largely owing to the following evidence: (i) the overwhelming intensities of the CO_L bipolar peak throughout the studied potential range and (ii) neither CO oxidation nor the dehydrogenation reaction was found to take place at potentials lower than +0.20 V.

As for the PtPb (80:20) nanodendrites (Figure 6c), linearly bonded CO species (CO_L) still exists throughout the investigated potentials, identified through the inverted bipolar peaks near 2066 cm^{-1}. However, a CO_2 band centered at 2340 cm^{-1} develops simultaneously with an increase in the amplitude of the CO_L bipolar peak from −100 to +300 mV; yet from +400 to +600 mV, the intensity of the CO_2 band keeps increasing, accompanied by a shrinking in the amplitude of the CO_L bipolar peak. More importantly, a new series of bipolar peaks centered at 1720 cm^{-1}, likely ascribed to the carbonyl C═O stretching mode from $-COOH_{ads}$,[43] develops from 0.0 mV concurrently with the gradually intensifying amplitude of the CO_2 band. The bridge-bonded CO species (CO_B), previously seen as a negative-going band near 1815 cm^{-1} in the spectra of Pt particles and PtPb (95:5), completely vanishes in all spectra of PtPb (80:20). On one hand, the evidence of both the CO_L species and the

(38) Ranjan, C.; Hoffmann, R.; DiSalvo, F. J.; Abruna, H. D. *J. Phys. Chem. C* **2007**, *111*, 17357.
(39) Osawa, M. In *Advances in Electrochemical Science and Engineering*; Alkire, R. C., Kolb, D. M., Lipkowski, J., Ross, P. N., Eds.; Wiley-VCH: Weinheim, 2006; Vol. 9, p 269.
(40) Samjeské, G.; Miki, A.; Ye, S.; Osawa, M. *J. Phys. Chem. B* **2006**, *110*, 16559.
(41) Chen, W.; Sun, S.-G.; Zhou, Z.-Y.; Chen, S.-P. *J. Phys. Chem. B* **2003**, *107*, 9808.
(42) Chen, A.; La Russa, D. J.; Miller, B. *Langmuir* **2004**, *20*, 9695.
(43) Xia, X. H.; Liess, H.-D.; Iwasita, T. *J. Electroanal. Chem.* **1997**, *437*, 233.

$-COOH_{ads}$ species in the spectra strongly imply that the oxidation of formic acid on PtPb (80:20) nanodendrites proceeds via both dehydrogenation and dehydration pathways. On the other hand, the extinction of CO_B species provides solid evidence to show that the ensemble/ligand effect is brought by the crystal lattice dilation due to the incorporated 20 atom % of Pb. The early onset potential of formic acid oxidation and significantly enhanced current density at low potentials (<150 mV), which were observed in Figure 5, are therefore mainly due to the dehydrogenation reaction.

In the potential-dependent series of FTIR spectra of PtPb (50:50) nanodendrites (Figure 6d), no inverted bipolar CO peak is visible in the spectra at any potential, while the negative-going band corresponding to CO_2 can be observed even at the low potential of −100 mV. Moreover, the gaining of intensity of the CO_2 band under the incremental potentials was simultaneously accompanied with gradually intensified amplitude of the aforementioned bipolar C═O peaks centered at 1720 cm^{-1} from 0.0 to +600 mV, indicating that the detected CO_2 was solely produced from the $-COOH_{ads}$ species via the dehydrogenation reaction. This clearly demonstrates that the PtPb (50:50) nanodendrites are capable of electrochemically catalyzing the oxidation of formic acid, preferably through the dehydrogenation pathway, as a result of completely preventing CO from adsorbing on the PtPb intermetallic surface. This systematic study has presented direct spectroscopic evidence to illustrate that the modification of crystal structures may dramatically improve the electrocatalytic activity by altering the reaction mechanism. This demonstrates the great importance of developing and understanding a reproducible and controllable synthetic approach to tailor the desired intermetallic crystalline structure.

The synthetic method we employed herein is a wet chemistry route with the aid of a hydrothermal treatment. On one hand, the aqueous mixture in the solution phase allows precise control of the reaction stoichiometry and, subsequently, precise control of the intermetallic composition. On the other hand, hydrothermal processes can initiate nucleation of nanocrystals and promote the formation of crystalline products at temperatures substantially lower than those required by conventional solid-state or vapor-phase reactions. Combining the advantages of such strategies has armed us with control over the crystalline structure and compositions. From the time-dependent experiments (Figure 7), some insights have been gained on the hydrothermal reaction mechanism through using ex situ SEM to monitor the formed deposits at different reaction stages. Parts a and d of Figure 7 display the SEM images taken on the produced deposits of PtPb (95:5) and PtPb (50:50) systems, respectively, during the initial mixing and heating until ca. 10 min. It is reasonable to speculate that, at this stage, formic acid mainly serves as a reducing agent to produce the observed numerous nanoclusters as seeds for further crystal nucleation and growth. After the hydrothermal reaction had proceeded for a certain period of time (ca. 30 min, Figure 7b,e), those nucleating nanoclusters grew larger, giving rise to some

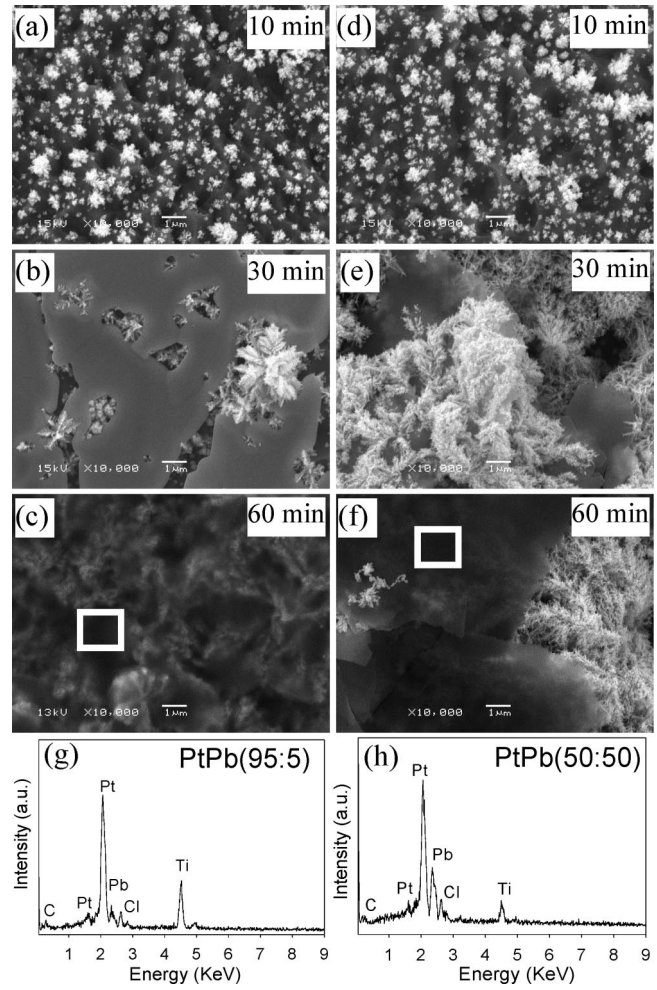

Figure 7. SEM images taken at different hydrothermal reaction times: (a−c) PtPb (95:5) and (d−f) PtPb (50:50). The EDS spectra recorded from the spots indicated by the white squares on images c and f are shown in g and h, respectively. All scale bars in images a−f are 1 μm.

prototypical dendritic patterns and structures. In particular, gel-like solid materials are found with those dendritic deposits embedded therein. When the hydrothermal process proceeded, after 60 min (Figure 7c,f), the gel-like material was found as a coating layer grown on the top of the PtPb (95:5) dendrites and (50:50) fractal-like filaments. Quantitative EDS analysis, shown in Figure 7g,h, reveals that such gel-like solid media always contain Pt, Pb, Cl, and C with an average atomic ratio of [Pt + Pb]:Cl:C = 1:*b*:*a*, where *a* and *b* can be roughly rounded to 1 or 2, respectively. Suggested from the coordination chemistry involving Pt cations with carboxyl ligands, the origin of the gel-like solid media can be speculated to be that when large amounts of incoming $PtCl_6^{2-}$ and Pb^{2+} ions were encountered by formate ($HCOO^-$) ligands around the interface of nanoclusters and solution, a partial replacement of Cl^- ligands by $HCOO^-$ ligands for $PtCl_6^{2-}$ and the coordination of $HCOO^-$ ligands with Pb^{2+} cations may give rise to the metastable chelated species $[Cl_bPt_x-(HCOO)_a-Pb_{100-x}]^{Z-}$ as a kinetic product. Therefore, the observed gel-like solid media, originating from the metastable complex $[Cl_bPt_x-(HCOO)_a-Pb_{100-x}]^{Z-}$, may exist as a highly condensed phase coated on the surface of the initial nucleation centers. Continued heating treatment further triggered the direct intramolecular electron transfer

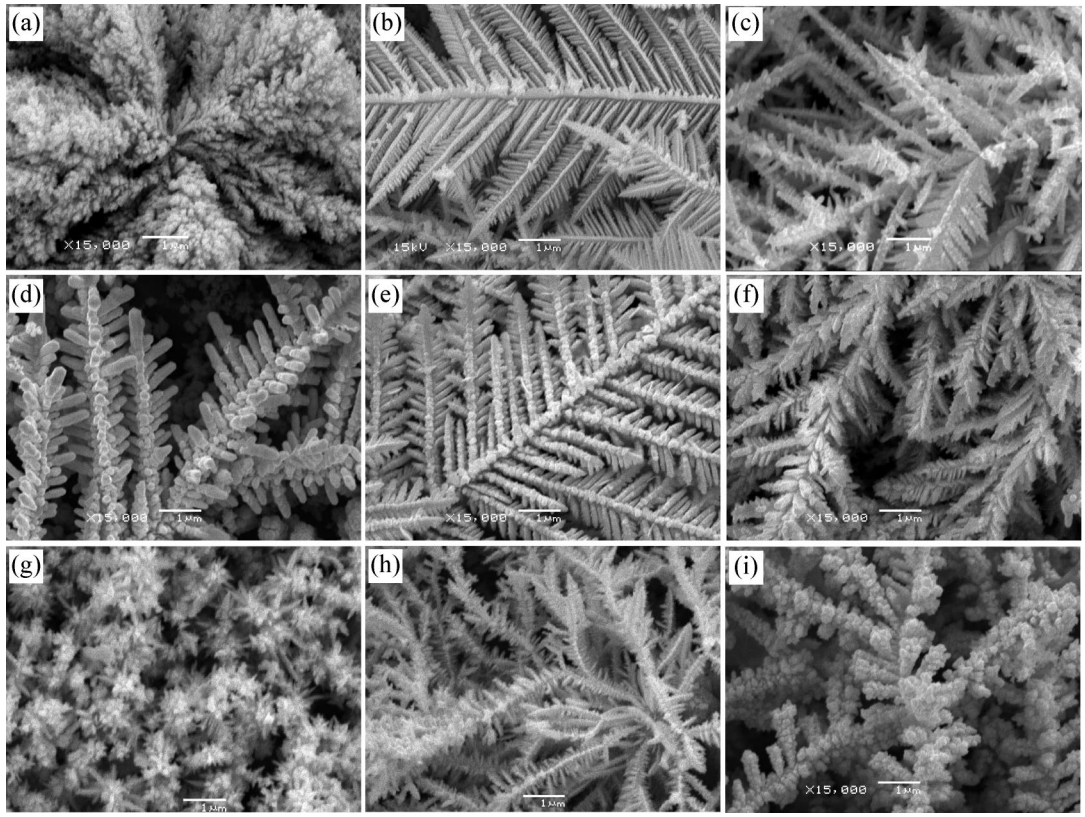

Figure 8. Dendritic nanostructures achieved from a wide range of intermetallics. SEM images of various as-synthesized Pt-containing nanodendrites of different compositions: (a) PtAu (95:5), (b) PtAu (5:95), (c) PdRu (90:10), (d) PtBi (95:5), (e) PtBi (70:30), (f) PtBi (50:50), (g) PtPd (2:98), (h) PtPd (20:80), and (i) PtPd (50:50). All scale bars are 1 μm.

from carbon atoms to metal cores, thus producing reduced intermetallic compounds with desired composition, i.e. Pt_xPb_{100-x}. It is worth noting that when there are no Pb species present in the system, the complex $[Cl_bPt_x-(HCOO)_a]^{Z-}$ does not appear in the form of condensed gel media and is not seen throughout any reaction stage for the 100 atom % Pt system; instead, the intermediate complex is highly reactive and short-lived upon thermal treatment to produce agglomerated Pt particles. The important role of formate to the formation of the PtPb nanodentrites is further supported by the fact that only nanoporous PtPb networks were formed when formaldehyde was used as the reduction agent.[35]

With the aid of computational modeling, some important understandings of the dynamics of dendrite growth have been gained in the past.[44−48] It is believed that dendritic growth reflects a competition between order associated with the symmetries of the crystal structure and morphological instabilities arising from the nonlinear diffusion process.[47] In computer simulations of the morphology of a diffusion-limited aggregate, a change in the random noise level can vary the morphology from ordered anisotropic shape into an irregularly branching pattern.[44] In the present work, 100 atom % Pt species, when reduced, cannot produce dendritic morphology at all, while the presence of 2.5 atom % Pb is capable of massively triggering the dendritic growth. Therefore, the Pb atoms at a low percentage (e.g., 0.5 and 2.5 atom %) can be treated as "foreign impurities" with respect to the Pt matrix. This could correspond to the aforementioned "instabilities" in crystal growth and "random noise" in computer simulations, both of which are essentially important for inducing the dendritic growth. In the case of our hydrothermal process, the reducing agent formic acid is always present in large excess compared to the metal precursors. This ensures the coreduction of both metal cations and produces sufficiently fast reaction kinetics to cause supersaturation during the crystal nucleation phase. In the subsequent crystal growth phase, diffusion of the reduced Pt and Pb is the dominant driving force responsible for the dendritic growth. When small amounts of Pb (e.g., 0.5, 2.5, 5.0 atom %) are introduced, the reduced Pb species serve as "pinning centers" and interfere with the growth front of the main trunks. Since the interfering Pb atoms have the possibility of occupying certain crystal lattice points during the diffusion process and the anisotropic growth of Pt atoms along the preferred crystal lattice is kinetically fast enough to engulf the Pb atoms and further accommodate these foreign atoms inside the crystal lattice, the formed intermetallic nanocrystals are always consistent in composition with the original aqueous mixture of inorganic precursors. In those cases with higher percentage of Pb (>5 atom %), the overall chemical and physical processes are expected to proceed similarly to those cases with low Pb contents, except that more reduced Pb atoms (foreign impurities) serve as "pinning

(44) Ben-Jacob, E.; Garik, P. *Nature (London)* **1990**, *343*, 523.
(45) Gránásy, L.; Pusztai, T.; Warren, J. A.; Douglas, J. F.; Borzsonyi, T.; Ferreiro, V. *Nat. Mater.* **2003**, *2*, 92.
(46) Haxhimali, T.; Karma, A.; Gonzales, F.; Rappaz, M. *Nat. Mater.* **2006**, *5*, 660.
(47) Imai, H. *Top. Curr. Chem.* **2007**, *270*, 43.
(48) Fleury, V. *Nature (London)* **1997**, *390*, 145.

centers" to deflect the growth front of the main trunks and give rise to more side branches, thus resulting in the less and less ordered dendrite morphology observed in Figure 1e−h. As for the PtPb (50:50) system, supersaturation and high concentrations of foreign particles are both responsible for the less ordered fractal-like morphology due to the ultrafast crystal growth rate and that the hexagonal crystal lattice is energetically stable enough to stack equimolar Pt and Pb atoms simultaneously.

Given the proposed dendritic growth mechanism, the method developed in this study can be a universal approach for fabricating a wide range of intermetallic nanodendrites, as long as the "foreign-particle-induced dendritic growth" can be triggered by the ultrafast hydrothermal coreduction of metal precursors. We further applied this method to synthesize a variety of intermetallic nanodendrites with different compositions. Parts a and b of Figure 8 present the SEM images of PtAu (95:5) and (5:95) nanostructures, respectively. The PtAu (95:5) nanodendrites apparently possess dense-branching morphology, while the PtAu (5:95) nanodendrites appear to be more symmetrical. In addition, for the first time, PdRu nanodendrites were synthesized at an atomic ratio of 90:10, as shown in Figure 8c. Parts d, e, and f of Figure 8 show the SEM images of dendritic PtBi (95:5), (70:30), and (50:50), respectively. These different bimetallic compositions produce three distinctive dendritic morphologies: the ordered rodlike side branches of PtBi (95:5) dendrites appear to have 3-fold symmetry without having tertiary branches, the ordered secondary branches of PtBi (70:30) dendrites tend to obey 2-fold symmetry with many ordered hierarchical subbranches, and PtBi(50:50) nanodendrites resemble the morphology of tip-splitting branchings, indicating a faster growth kinetics than the previous two. As for the PtPd system (Figure 8g−i), multiarmed globular dendrites were observed for PtPd (2:98) composition, and standard dendritic morphology was seen for PtPd (20:80) materials that possess ultralong primary trunks and relatively short secondary branches; PtPd (50:50) nanodendrites likely belong to a unique type of dense-branching morphology, in which both the trunks and the side branches appear to consist of grainy clusters. Even though the diversity in compositions and morphologies illustrated in Figure 8 are much richer than one could imagine, there is still one feature in common originating from our proposed dendritic growth mechanism: for both 50:50 compositions, the exhibited morphologies, as shown in Figure 8 f,i, appear to result from ultrafast crystal growth kinetics, which is likely caused by the underlying high supersaturation and a high amount of "foreign particles" involved in the tip-deflecting process.

Conclusion

In summary, these findings for the first time enrich our understanding toward the underlying mechanism of dendritic growth of intermetallic compounds. The developed hydrothermal synthetic method has proved to effectively fabricate intermetallic PtPb nanodendrites with controllable compositions and with unique electrocatalytic properties dependent on crystal structures. On the basis of understanding the underlying mechanism for dendritic growth of intermetallics, the hydrothermal synthetic approach and related strategies are highly promising as a universal approach for fabricating a wide range of intermetallic nanomaterials (binary or even ternary alloys). These intermetallic compounds with novel dendritic morphology are expected to have versatile scientific and technological applications, such as metal alloying and processing, surface plasmon-related research topics, design of novel bio- and chemical sensors, fuel cell catalyst development, and much more. In addition to their rich physical properties, the advanced hierarchical structures of the as-synthesized nanodendrites are expected to hold great potential for assembling hybrid functional nanodevices and nanosystems.

Acknowledgment. This work was supported by a Discovery Grant from the Natural Sciences and Engineering Research Council of Canada (NSERC). A.C. acknowledges the Canada Foundation of Innovation (CFI) and NSERC for the Canada Research Chair Award in Material and Environmental Chemistry.

CM9000174